

# Bayesian constraints on dark matter halo properties using gravitationally-lensed supernovae

N.V. Karpenka<sup>1\*</sup>, M.C. March<sup>2</sup>, F. Feroz<sup>3</sup> and M.P. Hobson<sup>3</sup>

<sup>1</sup>*The Oskar Klein Centre for Cosmoparticle Physics, Department of Physics, Stockholm University, AlbaNova, SE-106 91 Stockholm, Sweden*

<sup>2</sup>*Astronomy Centre, University of Sussex, Brighton BN1 9QH, UK*

<sup>3</sup>*Astrophysics Group, Cavendish Laboratory, JJ Thomson Avenue, Cambridge CB3 0HE, UK*

Accepted —. Received —; in original form 13 July 2012

## ABSTRACT

A hierarchical Bayesian method is applied to the analysis of Type-IA supernovae (SNIa) observations to constrain the properties of the dark matter haloes of galaxies along the SNIa lines-of-sight via their gravitational lensing effect. The full joint posterior distribution of the dark matter halo parameters is explored using the nested sampling algorithm MULTINEST, which also efficiently calculates the Bayesian evidence, thereby facilitating robust model comparison. We first demonstrate the capabilities of the method by applying it to realistic simulated SNIa data, based on the real 3-year data release from the Supernova Legacy Survey (SNLS3). Assuming typical values for the halo parameters in our simulations, we find that a catalogue analogous to the existing SNLS3 data set is incapable of detecting the lensing signal, but a catalogue containing approximately three times as many SNIa does produce robust and accurate parameter constraints and model selection results for two halo models: a truncated singular isothermal sphere (SIS) and a Navarro–Frenk–White (NFW) profile, thereby validating our analysis methodology. In the analysis of the real SNLS3 data, contrary to previous studies, we obtain only a very marginal detection of a lensing signal and weak constraints on the halo parameters for the truncated SIS model, although these constraints are tighter than those obtained from the equivalent simulated SNIa data set. This difference is driven by a preferred value of  $\eta \approx 1$  in the assumed scaling-law  $\sigma \propto L^\eta$  between velocity dispersion and luminosity, which is somewhat higher than the canonical values of  $\eta = \frac{1}{4}$  and  $\eta = \frac{1}{3}$  for early and late-type galaxies, respectively, and leads to a stronger lensing effect by the halo. No detection of a lensing signal is made for the NFW model.

**Key words:** gravitational lensing: weak – methods: data analysis – methods: statistical – supernovae: general – galaxies: haloes

## 1 INTRODUCTION

In using Type Ia supernovae (SNIa) as ‘standardizable’ candles to constrain cosmological parameters, one typically assumes that the universe is homogeneous and isotropic, and therefore one ignores gravitational lensing effects due to cosmic structure along the line-of-sight to each SNIa. In conventional cosmological SNIa analyses, this effect is usually regarded as an additional source of uncertainty, which adds extra scatter to the brightness of SNIa that increases with redshift (Kantowski et al. 1995, Frieman 1996, Wambsganss et al. 1997, Holz & Wald 1998, Bergström et al. 2000). Fortunately, owing to flux conservation, the effects of gravitational magnification and demagnification average out and are therefore expected to lead to negligible bias in cosmological parameter estimates (see, e.g., Sarkar et al. 2008, Jönsson et al. 2008).

Nonetheless, the gravitational lensing of SNIa can itself be used to constrain cosmology (Metcalf 1999, Dodelson & Vailinotto 2006, Zentner & Bhattacharya 2009) and/or the properties of the lensing matter (Rauch 1991, Metcalf & Silk 1999). In the latter case, one performs a complementary analysis to cosmological parameter estimation by instead assuming a particular background cosmological model (i.e. fixing the cosmological parameters to some concordance values) and using the observed distance moduli to constrain the nature of the cosmic structure, such as the properties of dark matter haloes, along the lines-of-sight to the SNIa. In principle, one might even hope to perform a joint analysis to constrain the background cosmological parameters and the nature of the cosmic structure simultaneously, but such an approach is likely to suffer from strong degeneracies between parameters.

An early tentative detection of gravitational lensing of SNIa was made by Jönsson et al. (2007) using a sample from the Great Observatories Origins Deep Survey (GOODS; Riess et al. 2004, Strolger et al. 2004, Riess et al. 2007). More recently,

\* E-mail: nkarp@fysik.su.se

Kronborg et al. (2010) focussed on the detection of a gravitational lensing signal by assuming properties for dark matter haloes and reported a positive result at the 99 per cent confidence level. Moreover, Jönsson et al. (2010a) used 24 high-redshift ( $0.4 \lesssim z \lesssim 1.8$ ) SNIa from GOODS to constrain the properties of dark matter haloes of galaxies also contained within GOODS. This study was extended in Jönsson et al. (2010b) by using 175 high-redshift ( $0.1 \lesssim z \lesssim 1$ ) SNIa from the 3-year data release of the Supernova Legacy Survey (SNLS3; Astier et al. 2006) to constrain the haloes of galaxies in the deep Canada-France-Hawaii Telescope Legacy Survey (CFHTLS) fields. Although the SNIa in SNLS are typically not as distant as those from GOODS, they are far more numerous and selected in a more homogeneous way. Jönsson et al. (2010b) report the detection of a gravitational lensing signal at the 92 per cent confidence level.

In this paper, we also use high-redshift SNIa from SNLS3 to constrain the properties of dark matter haloes of galaxies in the CFHTLS fields that intersect the SNIa lines-of-sight. Our statistical methodology differs greatly, however, from that used by Jönsson et al. (2010a,b) and other previous studies. As recently discussed by March et al. (2011), the usual  $\chi^2$ -method used to constrain cosmological parameters and/or the nature of cosmic structure from lightcurve fits to SNIa observations (see e.g. Astier et al. 2006; Kowalski et al. 2008; Conley et al. 2011) suffers from some several shortcomings in terms of its statistical foundations and robustness, including not allowing for rigorous model checking and not providing a reliable framework for the evaluation of systematic uncertainties. Consequently, we instead analyse the SALT-II lightcurve fits of the SNIa observations using the statistically-principled and rigorous Bayesian hierarchical method (BHM) of March et al. (2011) to obtain a robust effective likelihood function giving the probability of obtaining the observed SNIa data (i.e. the parameter values obtained in the SALT-II lightcurve fits) as a function of the parameters of the dark matter halo models assumed for the galaxies along the lines-of-sight to the SNIa. Moreover, rather than exploring the parameter space of the dark matter halo models using simple gridding methods (see e.g. Jönsson et al. 2010a,b), we instead sample from the full joint posterior distribution of the dark matter halo parameters using a nested sampling algorithm (Skilling 2004; Feroz & Hobson 2008; Feroz et al. 2009). This enables us to explore all the halo model parameters simultaneously and allows for straightforward marginalisation over subsets of them. The algorithm also efficiently calculates the Bayesian evidence, thereby facilitating robust model comparison.

The outline of this paper is as follows. In Section 2 we give a brief summary of Bayesian inference methods, followed in Section 3 by a description of our Bayesian methodology for using gravitational lensing of SNIa to constrain the properties of dark matter haloes of the galaxies intersecting the lines-of-sight. In Section 4, we describe the SNLS3 supernovae and galaxies data used in our analysis. We test the performance of our Bayesian methodology in Section 5 by applying to realistic simulated data based on the real SNLS3 data, before analysing the real data sets and presenting our results in Section 6. We give our conclusions in Section 7.

Throughout the paper, we assume a spatially-flat concordance  $\Lambda$ CDM background cosmology, characterised by the parameters  $\mathcal{C} \equiv \{\Omega_{m,0}, \Omega_{\Lambda,0}, H_0\} = \{0.27, 0.73, 0.7\}$ . Finally, we note that this paper may be considered as complementary to our companion paper (March et al. 2012), in which we use the BHM to analyse the SNLS3 catalogue, together with additional low-redshift SNIa, to constrain the background cosmological model, assuming no gravitational lensing along the lines-of-sight to the SNIa.

## 2 BAYESIAN INFERENCE

Our analysis methodology is built upon the principles of Bayesian inference, which provide a consistent approach to the estimation of a set of parameters  $\Theta$  in a model (or hypothesis)  $H$  for the data  $\mathbf{D}$ . Bayes' theorem states that

$$\Pr(\Theta|\mathbf{D}, H) = \frac{\Pr(\mathbf{D}|\Theta, H) \Pr(\Theta|H)}{\Pr(\mathbf{D}|H)}, \quad (1)$$

where, for brevity, we denote  $\Pr(\Theta|\mathbf{D}, H) \equiv P(\Theta)$  as the posterior probability distribution of the parameters,  $\Pr(\mathbf{D}|\Theta, H) \equiv \mathcal{L}(\Theta)$  as the likelihood,  $\Pr(\Theta|H) \equiv \pi(\Theta)$  as the prior, and  $\Pr(\mathbf{D}|H) \equiv \mathcal{Z}$  as the Bayesian evidence.

In parameter estimation, the normalising evidence factor is usually ignored, since it is independent of the parameters  $\Theta$ , and inferences are often obtained by taking samples from the (unnormalised) posterior using standard MCMC sampling methods, where at equilibrium the chain contains a set of samples from the parameter space distributed according to the posterior. This posterior constitutes the complete Bayesian inference of the parameter values, and can be marginalised over each parameter to obtain individual parameter constraints.

In contrast to parameter estimation problems, for model selection the evidence takes the central role and is simply the factor required to normalize the posterior over  $\Theta$ ,

$$\mathcal{Z} = \int \mathcal{L}(\Theta) \pi(\Theta) d^D \Theta, \quad (2)$$

where  $D$  is the dimensionality of the parameter space. As the average of the likelihood over the prior, the evidence is larger for a model if more of its parameter space is likely and smaller for a model with large areas in its parameter space having low likelihood values, even if the likelihood function is very highly peaked. Thus, the evidence automatically implements Occam's razor. The question of model selection between two models  $H_0$  and  $H_1$  can then be decided by comparing their respective posterior probabilities given the observed data set  $\mathbf{D}$ , as follows

$$R = \frac{\Pr(H_1|\mathbf{D})}{\Pr(H_0|\mathbf{D})} = \frac{\Pr(\mathbf{D}|H_1) \Pr(H_1)}{\Pr(\mathbf{D}|H_0) \Pr(H_0)} = \frac{\mathcal{Z}_1 \Pr(H_1)}{\mathcal{Z}_0 \Pr(H_0)}, \quad (3)$$

where  $\Pr(H_1)/\Pr(H_0)$  is the a priori probability ratio for the two models, which can often be set to unity but occasionally requires further consideration.

Evaluation of the multidimensional integral in Eq. (2) is a challenging numerical task. Standard techniques like thermodynamic integration are extremely computationally intensive which makes evidence evaluation at least an order of magnitude more costly than parameter estimation. Some fast approximate methods have been used for evidence evaluation, such as treating the posterior as a multivariate Gaussian centered at its peak (see e.g. Hobson & McLachlan 2003), but this approximation is clearly a poor one for multimodal posteriors (except perhaps if one performs a separate Gaussian approximation at each mode). The Savage-Dickey density ratio has also been proposed (see e.g. Trotta 2007) as an exact, and potentially faster, means of evaluating evidences, but is restricted to the special case of nested hypotheses and a separable prior on the model parameters. Various alternative information criteria for astrophysical model selection are discussed by Liddle (2007), but the evidence remains the preferred method.

The nested sampling approach, introduced by Skilling (2004), is a Monte Carlo method targeted at the efficient calculation of the evidence, but also produces posterior inferences as a by-product. Feroz & Hobson (2008) and Feroz et al. (2009) built on this nested

sampling framework and have introduced the MULTINEST algorithm which is very efficient in sampling from posteriors that may contain multiple modes and/or large (curving) degeneracies and also calculates the evidence. This technique greatly reduces the computational cost of Bayesian parameter estimation and model selection and has already been applied to a number of problems in astrophysics (see e.g. Feroz & Hobson 2011; Feroz et al. 2011; Bridges et al. 2009; Feroz et al. 2010). We employ this technique in this paper.

### 3 ANALYSIS METHODOLOGY

#### 3.1 Definition of the SNIa data

In practice, there are no perfect astronomical standard candles. In particular, SNIa have absolute magnitudes that vary by about  $\pm 0.8$  mag in the  $B$ -band due to physical differences in how each supernova is triggered and also due to absorption by its host galaxy. Nonetheless, SNIa do constitute a set of ‘standardizable’ candles, since by applying small corrections to their absolute magnitudes, derived by fitting multi-wavelengths observations of their lightcurves, one can reduce the scatter considerably, to around  $\pm 0.15$  mag in the  $B$ -band. In essence, SNIa with broader light curves and slower decline rates are intrinsically brighter than those with narrower light curves and fast decline rates (Phillips 1993).

Several methods are available for fitting SNIa lightcurves (and constraining cosmological parameters), including, amongst others, the Multi-Colour Lightcurve Shape (MCLS) strategy (Jha et al. 2007), CMAGIC (Wang et al. 2003; Conley et al. 2006), and the Spectrally Adaptive Lightcurve Template (SALT) method (Guy et al. 2007), the current version of which is SALT-II. The relative merits of these methods is a topic of much debate, but the SALT-II method is particularly attractive for our purposes, since (unlike MCLS) it first fits each SNIa lightcurve to obtain three parameters controlling the SN magnitude, stretch and colour corrections to a template ‘learned’ from nearby and distant SN; only in a second, separate step are these fits used to constrain cosmological parameters. Following March et al. (2011), we may therefore use the products of the first step as the inputs to a statistically rigorous Bayesian hierarchical model.

Our analysis takes place after the selection cuts, lightcurve fitting and Malmquist correction have been performed. For each selected SNIa, in addition to an estimate  $\hat{z}$  of its redshift and an associated uncertainty  $\sigma_z$ , derived from observations of its host galaxy, we take as our basic data the output from the SALT-II lightcurve fitting algorithm, which produces the best-fit values:  $\hat{m}_B^*$ , the rest frame  $B$ -band apparent magnitude of the supernovae at maximum luminosity;  $\hat{x}_1$ , the stretch parameter related to the width of the fitted light curve; and  $\hat{c}$ , the colour excess in the  $B$ -band at maximum luminosity. These are supplemented by the covariance matrix of the uncertainties in the estimated lightcurve parameters, namely

$$\hat{C} = \begin{pmatrix} \sigma_{m_B^*}^2 & \sigma_{m_B^*,x_1} & \sigma_{m_B^*,c} \\ \sigma_{m_B^*,x_1} & \sigma_{x_1}^2 & \sigma_{x_1,c} \\ \sigma_{m_B^*,c} & \sigma_{x_1,c} & \sigma_c^2 \end{pmatrix}. \quad (4)$$

Therefore, our basic input data for each SN ( $i = 1, \dots, N_{\text{SN}}$ ) are

$$D_i \equiv \{\hat{z}_i, \hat{m}_{B,i}^*, \hat{x}_{1,i}, \hat{c}_i\}, \quad (5)$$

and we assume (as is implicitly the case throughout the SNe literature) that the vector of values  $(\hat{m}_{B,i}^*, \hat{x}_{1,i}, \hat{c}_i)$  for each SN is distributed as a multivariate Gaussian about the true values, with

covariance matrix  $\hat{C}_i$ . The ‘observed’ distance modulus  $\mu_i^{\text{obs}}$  for each SN is then modelled as

$$\mu_i^{\text{obs}} = \hat{m}_{B,i}^* - M_i + \alpha \hat{x}_{1,i} - \beta \hat{c}_i, \quad (6)$$

where  $M_i$  is the (unknown)  $B$ -band absolute magnitude of the SN, and  $\alpha, \beta$  are (unknown) nuisance parameters (assumed the same for all SN) controlling the stretch and colour corrections.

It should be noted that a sophisticated Bayesian hierarchical method has recently been proposed by Mandel et al. (2009, 2010) to fit optical and infrared lightcurve data. This may provide a more robust technique for defining the basic SNIa data that we use in our subsequent analysis, but we leave the investigation of this issue to a future work.

#### 3.2 Computing the predicted distance moduli

In using SNIa to constrain cosmic structure, the predicted distance modulus must include the effect of gravitational magnification due to cosmic structure along the line-of-sight to each supernova. In particular, we assume this magnification is due to dark matter haloes associated with known galaxies intersecting the line-of-sight. Thus, for each SNIa, the predicted magnification depends on the sets of parameters  $\{\mathbf{g}, \mathbf{h}\}$ , where

$$\mathbf{g} = \{z_{\text{gal}}^1, \boldsymbol{\theta}_{\text{gal}}^1, M_B^1, \tau^1, \dots, z_{\text{gal}}^{N_{\text{gal}}}, \boldsymbol{\theta}_{\text{gal}}^{N_{\text{gal}}}, M_B^{N_{\text{gal}}}, \tau^{N_{\text{gal}}}\} \quad (7)$$

contains the redshift, sky position, absolute  $B$ -band magnitude and spectral type of the  $N_{\text{gal}}$  galaxies that intersect the line-of-sight to the SNIa, and  $\mathbf{h}$  contains the parameters of the assumed dark matter halo model for these galaxies (see Section 3.3). In general, the parameters  $\mathbf{g}$  are (naturally) different for each SN and are assumed known; one wishes to place constraints on the unknown halo parameters  $\mathbf{h}$ , which (perhaps unrealistically) are assumed common to all the foreground galaxies.

To compute the predicted magnification of a SNIa, we use the weak-lensing approximation (see, e.g., Schneider et al. 1992), the validity of which was checked by Jönsson et al. (2010b) by comparing it with a ray-tracing algorithm. For the SNIa sample we consider here (see Section 4.1), which have relatively low redshifts, the weak-lensing approximation was found to be accurate to within  $\sim 5$  per cent. In this approximation, the predicted distance modulus of a SNIa, expressed in terms of magnitudes, is related to the convergence  $\kappa$  along its line-of-sight by

$$\mu(z, \mathcal{C}, \mathbf{g}, \mathbf{h}) \approx \mu_0(z, \mathcal{C}) - 2.17[\kappa_{\text{los}}(\mathbf{g}, \mathbf{h}) - \kappa_{\text{b}}(\mathbf{h})], \quad (8)$$

where  $\mu_0(z, \mathcal{C})$  is the predicted distance modulus for our assumed cosmological parameters  $\mathcal{C}$ , neglecting gravitational lensing,  $\kappa_{\text{los}}(\mathbf{g}, \mathbf{h})$  is a sum over the contributions to the convergence from each galaxy along the line-of-sight, so that  $\kappa_{\text{los}} = \sum_{j=1}^{N_{\text{gal}}} \kappa_{\text{gal}}^j$ , and  $\kappa_{\text{b}}(\mathbf{h})$  represents the compensating effect of the background density and acts as a normalisation allowing the magnification relative to a homogeneous universe to be computed (Jönsson et al. 2010b). Flux conservation implies that  $\langle \kappa \rangle = 0$  and to ensure this condition is satisfied we set  $\kappa_{\text{b}}(\mathbf{h}) = \langle \kappa_{\text{los}}(\mathbf{g}, \mathbf{h}) \rangle$ , where the latter is calculated using a large number of randomly selected lines-of-sight.

#### 3.3 Halo models

Our primary goal is to constrain the parameters  $\mathbf{h}$  that describe the properties of the dark matter haloes associated with the galaxies

along the lines-of-sight to the SNIa. We assume that each galaxy contributes to the convergence by an amount

$$\kappa_{\text{gal}}(\xi) = \frac{\Sigma(\xi)}{\Sigma_c}, \quad (9)$$

where the surface density,  $\Sigma(\xi)$ , is obtained by projecting the matter distribution onto a lens plane,

$$\Sigma(\xi) = \int_{-\infty}^{\infty} \rho(\xi, y) dy, \quad (10)$$

where  $\xi$  is a vector in the plane and  $y$  is a coordinate along the line of sight; it is at this point that the density profile  $\rho(r)$  of the dark matter halo enters the calculation. The denominator in (9) is the critical surface density,

$$\Sigma_c = \frac{c^2}{4\pi G} \frac{D_s}{D_l D_{ls}}, \quad (11)$$

which, in turn, depends on the angular diameter distances between the observer and the source,  $D_s$ , the observer and the lens,  $D_l$ , and the lens and the source,  $D_{ls}$ . These distances are computed from the redshifts of the SN and galaxy respectively, assuming our concordance background cosmology.

In this paper, we investigate two different models for the density profile  $\rho(r)$  of the dark matter halo: the truncated singular isothermal sphere (SIS) and the NFW profile (Navarro et al. 1997), both of which we now describe.

### 3.3.1 Truncated singular isothermal sphere

The radial density distribution of a singular isothermal sphere (SIS) is given by

$$\rho(r) = \frac{\sigma^2}{2\pi G} \frac{1}{r^2}, \quad (12)$$

which depends on the single free parameter  $\sigma$ , the one-dimensional velocity dispersion of its constituent particles. Since the SIS profile has a divergent total mass, we truncate it at a radius  $r = r_t$ , which is thus a second free parameter.

The surface density of a truncated SIS is easily calculated using (10) and found to be

$$\Sigma(\xi) = \begin{cases} \frac{\sigma^2}{\pi G \xi} \arctan \sqrt{r_t^2/\xi^2 - 1} & \text{if } \xi \leq r_t \\ 0 & \text{if } \xi > r_t, \end{cases} \quad (13)$$

which can, in turn, be substituted into (9) to obtain the convergence  $\kappa_{\text{gal}}(\xi)$  due to the galaxy dark matter halo.

To allow for and investigate the relationship between galaxy luminosity and velocity dispersion, we follow Jönsson et al. (2010b) and adopt the Faber-Jackson (Faber & Jackson 1976) and Tully-Fisher-like (Tully & Fisher 1977) scaling law

$$\sigma = \sigma_* \left( \frac{L}{L_*} \right)^\eta, \quad (14)$$

where  $L_*$  is a fiducial luminosity, which we take to be  $L_* = 10^{10} h^{-2} L_\odot$  in the  $B$ -band, and  $\sigma_*$  is the corresponding fiducial velocity dispersion. In terms of absolute  $B$ -band magnitudes, with which we will be working, the scaling relation becomes

$$\sigma = \sigma_* 10^{-\eta(M_B - M_B^*)/2.5}, \quad (15)$$

where  $M_B^* = -19.52 + 5 \log_{10} h$  and  $h$  is the Hubble constant in units of  $100 \text{ km s}^{-1} \text{ Mpc}^{-1}$ . The (aperture) mass-to-light ratio of the galaxies is determined by  $\eta$ , since

$$\frac{M(r \leq R)}{L} = \frac{2\sigma_*^2 (L/L_*)^{2\eta} R}{G L} \propto L^{2\eta-1}, \quad (16)$$

provided  $R \leq r_t$ . Thus, for example, one has a constant mass-to-light ratio  $M/L \propto L^0$  if  $\eta = 0.5$ .

For the truncation radius, we again follow Jönsson et al. (2010b) and assume it obeys a scaling law of the form

$$r_t = r_* \left( \frac{\sigma}{\sigma_*} \right)^\gamma = r_* \left( \frac{L}{L_*} \right)^{\eta\gamma}, \quad (17)$$

where  $r_*$  is a fiducial truncation radius. Since we only include galaxies located a distance  $\theta_c$  from the position of the SN Ia, the truncation radius has an effect only if  $r_t/D_d < \theta_c$ . For  $\theta_c = 60''$  and  $z_{\text{gal}} < 1$  this corresponds to  $r_t \lesssim 300 h^{-1} \text{ kpc}$ .

Thus, for the truncated SIS halo model, we wish to constrain the four parameters  $\mathbf{h} = \{\gamma, \eta, \sigma_*, r_*\}$ .

### 3.3.2 Navarro–Frenk–White profile

The radial density distribution of the Navarro–Frenk–White (NFW) profile is given by

$$\rho(r) = \frac{\delta_c \rho_c}{(r/r_s)(1+r/r_s)^2}, \quad (18)$$

where  $\rho_c = 3H^2(z)/8\pi G$  is the critical density for closure of the universe at the redshift,  $z$ , of the halo and  $H(z)$  is the Hubble parameter at that same redshift. The scale radius  $r_s = r_{200}/c$  is a characteristic radius of the cluster, where  $c$  is a dimensionless number known as the concentration parameter, and

$$\delta_c = \frac{200}{3} \frac{c^3}{\ln(1+c) - c/(1+c)^{-1}} \quad (19)$$

is a characteristic overdensity for the halo. The virial radius,  $r_{200}$ , is defined as the radius inside which the mass density of the halo is equal to  $200\rho_c$ . The profile therefore depends on two free parameters: the virial radius  $r_{200}$  and the concentration parameter  $c$ . The mass of an NFW halo contained within the radius  $r_{200}$  is

$$M_{200} \equiv M(r \leq r_{200}) = \frac{800\pi}{3} \rho_c r_{200}^3 = \frac{800\pi}{3} \frac{\rho_m}{\Omega_m} r_{200}^3, \quad (20)$$

where  $\rho_m$  is the mean matter density of the universe and  $\Omega_m$  is the matter density parameter at the redshift  $z$  of the halo.

The surface density of the NFW profile is given by (Bartelmann 1996)

$$\Sigma(\xi) = \begin{cases} \frac{2r_s \delta_c \rho_c}{(x^2-1)} \left[ 1 - \frac{2}{\sqrt{1-x^2}} \operatorname{arctanh} \sqrt{\frac{1-x}{1+x}} \right] & (x < 1) \\ \frac{2r_s \delta_c \rho_c}{3} & (x = 1) \\ \frac{2r_s \delta_c \rho_c}{(x^2-1)} \left[ 1 - \frac{2}{\sqrt{x^2-1}} \arctan \sqrt{\frac{x-1}{x+1}} \right] & (x > 1) \end{cases} \quad (21)$$

where  $x = \xi/r_s$  is a dimensionless projected radial distance in the lens plane. Once again, this expression may be substituted into (9) to obtain the convergence  $\kappa_{\text{gal}}(\xi)$  due to the galaxy dark matter halo.

By analogy with the Tully–Fisher and Faber–Jackson relations, to allow for and investigate the relationship between the galaxy luminosity and the virial radius in a similar manner to the truncated SIS profile, we follow Jönsson et al. (2010b) and Kleinheinrich et al. (2004) and adopt the scaling law

$$r_{200} = r_{200}^* \left( \frac{L}{L_*} \right)^\lambda, \quad (22)$$

where, once again,  $L_*$  is a fiducial luminosity that we take to be

$L_* = 10^{10} h^{-2} L_\odot$  in the  $B$ -band, and  $r_{200}^*$  is the corresponding fiducial virial radius. The virial mass-to-light ratio is thus given by

$$\frac{M_{200}}{L} = \frac{800\pi}{3} \rho_c \frac{r_{200}^3}{L} \propto L^{3\eta-1}. \quad (23)$$

For example, a constant mass-to-light ratio  $M/L \propto L^0$  requires  $\lambda = \frac{1}{3}$ .

Thus, for the NFW halo model, we wish to constrain the three parameters  $\mathbf{h} = \{\lambda, c, r_{200}^*\}$ .

### 3.4 Likelihood function

To construct the likelihood function for the SNIa data, we adopt the Bayesian hierarchical model proposed by March et al. (2011). This has been shown to deliver tighter constraints on cosmological parameters than the usual  $\chi^2$ -method, and simultaneously provides a robust statistical framework for the full propagation of systematic uncertainties to the final inferences.

For the  $i$ th SN, we require the likelihood of the input data (5) given the parameters of our model, namely

$$\Pr(\hat{m}_{B,i}^*, \hat{x}_{1,i}, \hat{c}_i, \hat{z}_i | \mathbf{h}, \alpha, \beta, \sigma_{\text{int}}), \quad (24)$$

which also depends on the cosmological parameters  $\mathcal{C}$ , the covariance matrix  $\hat{C}_i$  of the uncertainties on the input data  $(\hat{m}_{B,i}^*, \hat{x}_{1,i}, \hat{c}_i)$ , and the uncertainty  $\sigma_{z,i}$  in the estimated redshift  $\hat{z}_i$ , all of which are assumed known. In particular, we seek to constrain the unknown halo parameters  $\mathbf{h}$ , global colour and stretch correction multipliers  $\alpha$  and  $\beta$ , and the intrinsic dispersion  $\sigma_{\text{int}}$  of SNIa absolute magnitudes (all of these are assumed to be ‘global’ parameters, i.e. common to every SN). Finally, the full likelihood function is given by the product of the likelihoods (24) for each SN.

Following March et al. (2011), we compute the likelihood (24) for each SN by first introducing the hidden variables  $M_i$ ,  $x_i$ ,  $c_i$  and  $z_i$ , which are, respectively, the true (unknown) values of its absolute  $B$ -band magnitude, stretch and colour corrections, and redshift. These are then assigned priors, which themselves contain further nuisance parameters, and all the introduced parameters are marginalised over to obtain the likelihood (24). The details of this procedure are given in Appendix A of our companion paper (March et al. 2012). By assuming separable Gaussian priors on the hidden variables and nuisance parameters, one can perform all the marginalisations analytically, except for two nuisance parameters  $R_x$  and  $R_c$  that must be marginalised over numerically. The full likelihood function thus depends on the parameters  $\Theta = \{\mathbf{h}, \alpha, \beta, \sigma_{\text{int}}, R_x, R_c\}$ , and is 9-dimensional for the truncated SIS halo model and 8-dimensional for the NFW profile model.

### 3.5 Priors on the sampled parameters

To determine the Bayesian inference problem completely, it only remains to specify the prior  $\pi(\Theta)$  on the parameters to be sampled. The choice of prior is particularly important for weak lensing analyses, since the problem is inherently underconstrained and therefore any prior information available is extremely useful. One should, however, be careful in the choice of priors not to impose too strong assumptions, which may lead to erroneous inferences.

Following March et al. (2011), we adopt the separable priors listed in Table 1 on each of the ‘non-halo’ (nuisance) parameters  $\sigma_{\text{int}}$ ,  $\alpha$ ,  $\beta$ ,  $R_x$  and  $R_c$ . On the halo parameters  $\mathbf{h}$ , the priors for each model are listed in Table 2, and correspond to broad, conservative assumptions.

Nuisance parameter	Symbol	Value
<i>SNIa population</i>		
Dispersion of absolute magnitude	$\sigma_{\text{int}}$	$\mathcal{U}(-3, 0)$ on $\log \sigma_{\text{int}}$
<i>Lightcurve</i>		
Stretch multiplier	$\alpha$	$\mathcal{U}(0, 4)$
Colour multiplier	$\beta$	$\mathcal{U}(0, 4)$
Dispersion of stretch correction	$R_x$	$\mathcal{U}(-5, 2)$ on $\log R_x$
Dispersion of colour correction	$R_c$	$\mathcal{U}(-5, 2)$ on $\log R_c$

**Table 1.** Priors on nuisance parameters, where  $\mathcal{U}(a, b)$  denotes a uniform distribution between the limits  $a$  and  $b$ .

Halo parameter	Symbol	Prior
<i>Truncated SIS halo</i>		
Fiducial velocity dispersion ( $\text{km s}^{-1}$ )	$\sigma_*$	$\mathcal{U}(0, 300)$
Fiducial truncation radius (Mpc)	$r_*$	$\mathcal{U}(0, 0.4)$
Exponent of $\sigma$ - $L$ power law	$\eta$	$\mathcal{U}(-5, 5)$
Exponent of $r_t$ - $\sigma$ power law	$\gamma$	$\mathcal{U}(-5, 5)$
<i>NFW profile halo</i>		
Concentration	$c$	$\mathcal{U}(0, 100)$
Fiducial virial radius (Mpc)	$r_{200}^*$	$\mathcal{U}(0, 0.4)$
Exponent of $r_{200}$ - $L$ power law	$\lambda$	$\mathcal{U}(-2, 2)$

**Table 2.** Priors on halo parameters for the truncated SIS and NFW models respectively.

## 4 SUPERNOVAE AND GALAXIES DATA SETS

To apply the Bayesian analysis methodology described above to constrain the dark matter haloes of galaxies, we need observations both of supernovae and foreground galaxies. As in Jönsson et al. (2010b), we use high-redshift ( $0.1 \lesssim z \lesssim 1$ ) SNIa from the 3-year SNLS data set (Guy et al. 2010) to constrain the properties of dark matter haloes of galaxies in the CFHTLS fields that intersect the SNIa lines-of-sight.

The SNLS consists both of photometric and spectroscopic observations. The photometry is obtained as part of the deep component of CFHTLS with the one square-degree imager MegaCam (Boulade et al. 2003). The deep part of CFHTLS comprises four fields (D1, D2, D3 and D4), each  $\approx 1 \text{ deg}^2$  in size, imaged in  $u^*$ ,  $g'$ ,  $r'$ ,  $i'$  and  $z'$  filters approximately every 4–5 days during dark and grey time, suitable for detecting supernovae and building light curves (Astier et al. 2006; Guy et al. 2010). The spectroscopic observations are used to determine the nature of the supernovae candidates and measure their redshifts (Howell et al. 2005; Bronder et al. 2008; Balland et al. 2009).

### 4.1 Supernovae

Our initial sample consisted of 230 high-redshift ( $0.1 \lesssim z \lesssim 1$ ) SNIa from the 3-year SNLS data set (Guy et al. 2010). We note that this is 13 fewer than used by Jönsson et al. (2010b), since these SNIa were excluded from the SALT-II fits for various reasons described in Conley et al. (2011), and do not appear in the tables in that paper. The sample of 230 SNIa is further reduced, however, by edge effects and by some parts of the deep CFHTLS fields being covered by bright stars that have to be masked (Sullivan et al. 2006). SNIa located too close to the boundary of the field or to a masked region are removed from the sample because of the lack of observations of foreground galaxies. Details of this procedure are given in Jönsson et al. (2010b). Only 162 of the initial sample of 230 SNIa fulfilled this selection criterion.

To compute the predicted magnification due to the foreground

galaxies along the line-of-sight to each SNIa, we require an estimate of its sky location  $\theta_{\text{SN}}$  and redshift  $\hat{z}_{\text{SN}}$ . The sky location is obtained from the CFHTLS  $i'$ -band photometry. When available,  $\hat{z}$  is taken to be the spectroscopic redshift of the SNIa host galaxy; otherwise the spectroscopic redshift of the SNIa itself is used.

Selection cuts, SALT-II lightcurve fitting and Malmquist corrections are made by the SNLS3 team and are already implemented in the supplied data files. As described in Section 3.1, the SALT-II fitting algorithm is applied to each SNIa lightcurve to obtain best-fit estimates of:  $\hat{m}_B^*$ , the rest frame  $B$ -band apparent magnitude of the supernovae at maximum luminosity;  $\hat{x}_1$ , the stretch parameter of the fitted light curve; and  $\hat{c}$ , the colour excess in the  $B$ -band at maximum luminosity. These are supplemented by the covariance matrices  $\hat{C}$  of the uncertainties in the estimated lightcurve parameters, which are taken from Conley et al. (2011).

## 4.2 Galaxies

Our foreground galaxies are taken from the SNLS galaxy catalogues in the deep CFHTLS fields. As discussed in Section 3.2, to perform our analysis we require for each galaxy: the redshift  $z_{\text{gal}}$ , sky position  $\theta_{\text{gal}}$ , absolute  $B$ -band magnitude  $M_B$ , and spectral type  $\tau$ . The techniques used to obtain these galaxy properties are described in detail in Sullivan et al. (2006) and Jönsson et al. (2010b).

## 5 APPLICATION TO SIMULATED SUPERNOVAE DATA

In order to test our Bayesian analysis methodology, we first apply it to simulated SNIa data. First, SNIa photometric data in the absence of gravitational lensing were simulated and fitted using the publicly available SNANA package (Kessler et al. 2009), in an identical manner to that described in our companion paper (March et al. 2012). In summary, the data were simulated to match closely the SNLS3 data set (Guy et al. 2010) by using the SNLS3 co-added simulation library files (which are publicly available as part of the SNANA package), a coherent magnitude smearing of 0.12, and colour smearing. The colour smearing effect, or broad-band colour dispersion model, implemented in the data simulation is the EXPOL model described by fig. 8 of Guy et al. (2010), and the simulated Malmquist bias is based on fig. 14 of Perrett et al. (2010).

The SNANA SNIa data simulation is a two-stage process that mimics the real data collection and analysis process. The first stage is the simulation of photometric data in accordance with the characteristic instrument and survey properties of the SNLS3 survey using the SNLS3 simulation library files mentioned above. The second stage is the lightcurve fitting process in which the photometric data are fitted to SALT-II templates to give estimates of the SNIa absolute  $B$ -band magnitude  $\hat{m}_B$ , lightcurve stretch  $\hat{x}_1$  and colour  $\hat{c}$ . At this lightcurve fitting stage, basic cuts are made to discard SNIa with a low signal-to-noise ratio and/or too few observed epochs in sufficient bands. After the lightcurve fitting stage we make a redshift dependent magnitude correction to correct for the Malmquist bias; the correction is taken from a spline interpolation of table 4 in Perrett et al. (2010).

The resulting simulated SNIa are randomly distributed on the sky across the four SNLS3 fields, outside of our masked regions, and have a redshift distribution appropriate for the SNLS3 survey. The final stage of our simulation process adds the lensing contribution due to the (assumed) galaxy haloes along the line-of-sight to each SN. This is performed using the real SNLS galaxy catalogue,

Halo parameter	Symbol	Value
<i>Truncated SIS halo</i>		
Fiducial velocity dispersion	$\sigma_*$	120 km s <sup>-1</sup>
Fiducial truncation radius	$r_*$	0.07 Mpc
Exponent of $\sigma$ - $L$ power law	$\eta$	$\frac{1}{3}$
Exponent of $r_t$ - $\sigma$ power law	$\gamma$	0
<i>NFW profile halo</i>		
Concentration	$c$	20
Fiducial virial radius	$r_{200}^*$	0.15 Mpc
Exponent of $r_{200}$ - $L$ power law	$\lambda$	$\frac{1}{3}$

**Table 3.** Halo parameter values used in the generation of simulated gravitationally-lensed SNIa data.

by assuming each galaxy to have a halo described by either a SIS or NFW profile with the parameters listed in Table 3.

For the SIS model, the choice of the velocity dispersion  $\sigma_*$  and truncation radius  $r_*$  correspond to the best-fit values obtained by Jönsson et al. (2010b). The value  $\eta = \frac{1}{3}$  corresponds to the Tully–Fisher relation for late-type galaxies, which should make up the majority of the SNLS sample, since nearly 95 per cent of them are star-forming galaxies. We also assume  $\gamma = 0$ , which corresponds to a constant truncation radius  $r_t = r_*$ , i.e. independent of the velocity dispersion and luminosity of the galaxy.

For the NFW model, our choices of values for  $c$  and  $r_{200}^*$  are motivated in part by Springel et al. (2008), who performed a simulation of Milky Way sized haloes and calculated the  $c$  and  $r_{200}$  values for them. The  $r_{200}$  values for these haloes are given in their table 1, and  $c$  value for the main sub-halo is given in their table 2. Typically, they find  $r_{200} \gtrsim 0.2$  Mpc and  $c \approx 10 - 16$ . We assume that most of galaxies in the SNLS sample are somewhat smaller than the Milky Way, and since it is well known that  $c$  is a decreasing function of mass, we assume  $c = 20$ , which yields a lensing signal of similar strength to that of our assumed truncated SIS halo. It should be noted, however, that the value of  $c$  in the simulations of Springel et al. (2008) varies with  $z$  and galaxy mass  $M$ , whereas we are assuming a fixed value for  $c$ , which is a naive assumption. We also assume that  $\lambda = \frac{1}{3}$ , which corresponds to a constant virial mass-to-light ratio  $M/L \propto L^0$ .

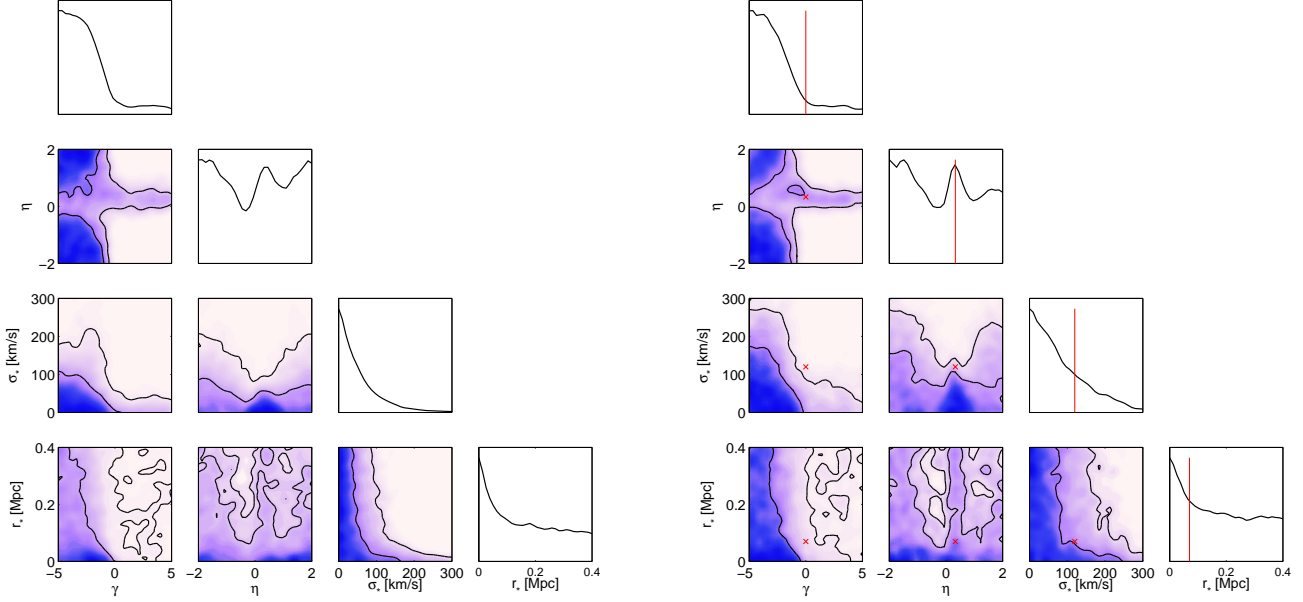
For an assumed set of halo properties, the lensing contribution from the haloes along the line-of-sight to each simulated SN is then added to the SN apparent magnitude, and its uncertainty is left unchanged.

## 5.1 Results for 162 simulated supernovae

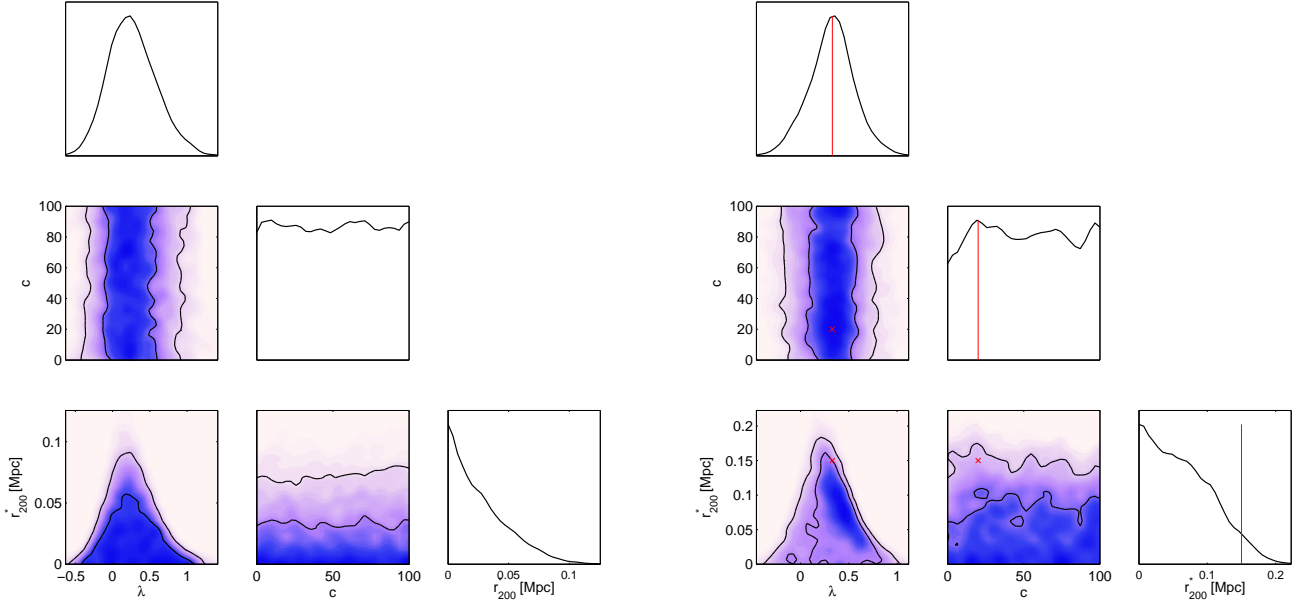
To match the real SNLS3 data to be analysed in Section 6, our first set of simulations contain 162 SNIa. Indeed, in this case, the positions on the sky of the simulated SNIa are fixed to those of the real SNLS3 SNIa.

Table 4 lists the Bayesian log-evidence for each combination of simulation and analysis model, relative in each case to the null (no-lensing) model. For each simulation model, one sees that the analysis model preferred by the Bayesian evidence is that assuming no lensing. This suggests that the quantity and quality of the real SNLS3 data to be analysed in Section 6 are insufficient to obtain a detection of the lensing signal, and certainly do not allow one to distinguish between different halo models.

For the four cases denoted by asterisks in Table 4, we plot the corresponding halo parameter constraints in Figs 1 and 2, respectively. From Fig. 1, one sees that, for the truncated SIS analysis model, the parameter constraints derived from simulated data with



**Figure 1.** 1D and 2D marginalised posteriors distributions for the parameters  $\mathbf{h} = \{\gamma, \eta, \sigma_*, r_*\}$  of the truncated SIS halo model, derived from the analysis of 162 simulated SNIa data generated assuming no lensing (left) and a truncated SIS model (right). In the right-hand panel, true parameters are indicated by vertical lines and crosses in 1D and 2D plots respectively.



**Figure 2.** 1D and 2D marginalised posteriors distributions for the parameters  $\mathbf{h} = \{\lambda, c, r_{200}^*\}$  of the NFW halo model, derived from the analysis of 162 simulated SNIa data generated assuming no lensing (left) and a truncated SIS model (right). In the right-hand panel, true parameters are indicated by vertical lines and crosses in 1D and 2D plots respectively.

Analysis model	Simulation model		
	No lensing	tSIS	NFW
No lensing	$0.0 \pm 0.2$	$0.0 \pm 0.2$	$0.0 \pm 0.2$
tSIS	$-1.8 \pm 0.2^*$	$-1.1 \pm 0.2^*$	$-1.3 \pm 0.2$
NFW	$-3.1 \pm 0.2^*$	$-2.6 \pm 0.2$	$-2.3 \pm 0.2^*$

**Table 4.**  $\Delta \log \mathcal{Z}$  (log-evidence value relative to the null evidence) for the analysis of simulated data with 162 SNIa. Asterisks denote the cases for which the corresponding halo parameters constraints are plotted in Figs 1 and 2, respectively.

and without a truncated SIS lensing signal are very similar, indicating that a SNLS-quality catalogue containing just 162 SNIa is insufficient to constrain the halo properties. In particular, we see that the 1D marginals for  $\sigma_*$  and  $r_*$  both peak at zero (which corresponds to no lensing signal). Another noteworthy feature is that, whereas the value of  $\eta$  is unconstrained, there is quite a strong constraint restricting  $\gamma$  to be negative. From (17), one sees that this corresponds to a rather curious truncation radius scaling-law, for which galaxies with larger velocity dispersions have smaller truncation radii. Moreover, provided  $\eta$  is positive, this also corresponds



Analysis model	Simulation model		
	No lensing	tSIS	NFW
No lensing	$0.0 \pm 0.2$	$0.0 \pm 0.2$	$0.0 \pm 0.2$
tSIS	$-1.7 \pm 0.2$	$4.5 \pm 0.2^*$	$6.9 \pm 0.2$
NFW	$-3.1 \pm 0.2$	$3.6 \pm 0.2$	$7.2 \pm 0.2^*$

**Table 5.**  $\Delta \log \mathcal{Z}$  (log-evidence value relative to the null evidence) for the analysis of simulated data with 500 SNIa. Asterisks denote the cases for which the corresponding halo parameters constraints are plotted in Figs 3 and 4, respectively.

to more luminous (and presumably more massive) galaxies having smaller truncation radii. This phenomenon was also noted by Jönsson et al. (2010b), but was erroneously interpreted as being a constraint on the halo properties derived from the SNIa data, which is clearly not the case since it occurs even in the analysis of simulations containing no lensing signal. Rather, from (13) and (17), one sees that a negative value of  $\gamma$  allows for a smaller value of the truncation radius  $r_t$  to ‘offset’ an increase in the velocity dispersion  $\sigma$ , thereby reducing the lensing signal produced by the putative halo, as required to be consistent with simulated data containing no lensing signal.

From Fig. 1, one also sees that the constraints on NFW halo parameters are almost identical when analysing data with and without the lensing signal. Once more, it is not possible to place constraints on the halo parameters. One should note, however, that the exponent  $\lambda$  of the scaling law between virial radius and luminosity does appear relatively well constrained around  $\lambda \approx \frac{1}{3}$ , which corresponds to a constant mass-to-light ratio  $M/L \propto L^0$ . Nonetheless, one sees a similar constraint when analysing simulated data containing no lensing signal; essentially, larger values of  $\lambda$  (through its dependence on  $r_{200}$ ) result in a stronger lensing signal that is ruled out by the data.

## 5.2 Results for 500 simulated supernovae

To test that our analysis procedure is capable of detecting the gravitational lensing signal and placing the correct constraints on halo parameters in presence of more data, we also analyse a simulated SNLS3-style catalogue containing 500 SNIa. In this case, the SNIa are randomly distributed on the sky over the four SNLS3 fields, outside of our masked regions. This simulated catalogue contains approximately three times the number of SNIa as considered previously and is thus representative of what could be achieved by the SLNS programme in a total of about 9 years of observation. This is clearly rather unrealistic in terms of the required observing time and resources, but still provides a useful insight into the quantity of SNIa data required to make a robust detection of the lensing signal and constrain halo properties.

Table 5 lists the Bayesian log-evidence for each combination of simulation and analysis model, relative in each case to the null (no-lensing) model. For the no-lensing simulation model, one sees that the no-lensing analysis model is again correctly preferred over both lensing halo models. More importantly, one now finds that for both simulations containing a lensing signal, the analysis models also containing a lensing signal are preferred at high significance, thereby indicating a robust detection of the gravitational lensing effect. Moreover, we note that in each case the correct halo model is preferred, although log-evidence differences between halo models are quite small, so this does not constitute a robust selection of the correct halo model.

For the two cases denoted by asterisks in Table 5, we plot

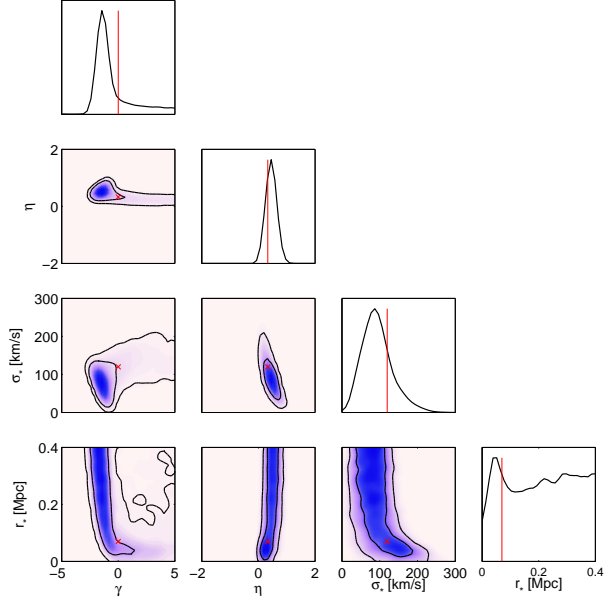


**Figure 3.** 1D and 2D marginalised posteriors distributions for the parameters  $\mathbf{h} = \{\gamma, \eta, \sigma_*, r_*\}$  of the truncated SIS halo model, derived from the analysis of 500 simulated SNIa data generated assuming a truncated SIS model. True parameters are indicated by vertical lines and crosses in 1D and 2D plots respectively.

the corresponding halo parameter constraints in Figs 3 and 4, respectively. From Fig. 3, which corresponds to a truncated SIS halo model in both the simulation and the analysis, one sees that each of the 1D and 2D marginalised posteriors has a well-defined peak (away from zero), indicating a robust detection of the lensing signal. This supports the conclusion drawn above from the Bayesian evidence results in Table 5. One also sees that all the parameters have been estimated with reasonable accuracy, although some of the 2D marginals exhibit pronounced degeneracies between the parameters, particular those involving the parameter  $r_*$ , which is the least well constrained.

Similar conclusions can be drawn from the parameter constraints corresponding to a NFW halo model in both the simulation and analysis, which are shown in Fig 4. One sees that the 1D and 2D marginalised distributions have reasonably well-defined peaks that contain the true parameter values, although again degeneracies do exist between parameters. One also sees that the 1D posteriors for both  $c$  and  $r_{200}^*$  peak well away from zero, supporting the conclusion drawn from the Bayesian evidences in Table 5 that one obtains a strong detection of the lensing signal.

## 6 APPLICATION TO REAL SUPERNOVAE DATA

We now apply our Bayesian analysis methodology to the real SNIa and galaxies data sets described in Section 4. For the real data we again consider both the truncated SIS and NFW halo models in our analysis. For each case, we also investigate dividing the foreground galaxies in the SNLS catalogue into passive and star-forming classes, each having halo model parameters that are allowed to be independent.

Table 4 lists the Bayesian log-evidence for each analysis model, relative in each case to the null (no-lensing) model. In the case of one galaxy type, one sees that there is a very marginal pref-



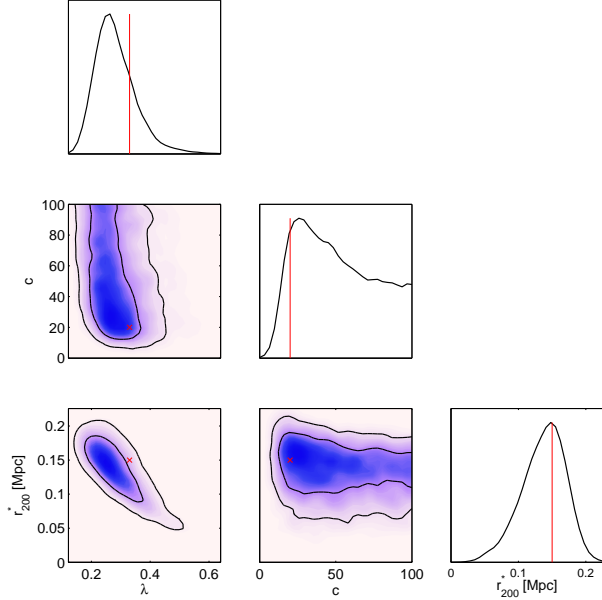


**Figure 4.** 1D and 2D marginalised posteriors distributions for the parameters  $\mathbf{h} = \{\lambda, c, r_{200}^*\}$  of the NFW halo model, derived from the analysis of 500 simulated SNIa data generated assuming a NFW model. True parameters are indicated by vertical lines and crosses in 1D and 2D plots respectively.

Model	1 galaxy type ( $\mathbf{h}^p = \mathbf{h}^{sf}$ )	2 galaxy types ( $\mathbf{h}^p \neq \mathbf{h}^{sf}$ )
Truncated SIS	$0.2 \pm 0.2^*$	$0.5 \pm 0.2^*$
NFW	$-2.5 \pm 0.2^*$	$-2.2 \pm 0.2$

**Table 6.**  $\Delta \log \mathcal{Z}$  (log-evidence value relative to the null evidence for no lensing signal) for the analysis of the real SNIa data.  $\mathbf{h}^p = \mathbf{h}^{sf}$  indicates that the halo parameters for passive and star-forming galaxies are constrained to be the same, whereas for  $\mathbf{h}^p \neq \mathbf{h}^{sf}$  they are allowed to be independent. Asterisks denote the cases for which the corresponding halo parameters constraints are plotted in Figs 5, 6 and 7, respectively.

t

erence of just 0.2 log-evidence units for a lensing signal produced by a truncated SIS halo model. This is, however, only at the level of the uncertainty in the evidence calculation, and so this model and the no-lensing model are broadly equally favoured. A lensing signal produced by a NFW halo model is, however, strongly disfavoured with an evidence of  $-2.5$  log-evidence units relative to the no lensing model.

When one splits the foreground galaxies into their passive and star-forming spectral types, one sees that the evidence for a lensing signal produced by a truncated SIS increases very slightly and is marginal preferred over the no lensing model by 0.5 log-evidence units. Once again, a lensing signal produced by a NFW halo model is quite strongly disfavoured by  $-2.2$  log-evidence units.

We discuss the halo parameters constraints for these various models in the following three subsections.

### 6.1 Truncated SIS model

The 1D and 2D marginalised parameter constraints obtained for the truncated SIS halo model with one galaxy type are shown in Fig. 5. As one might expect from the relative evidence for this model, the

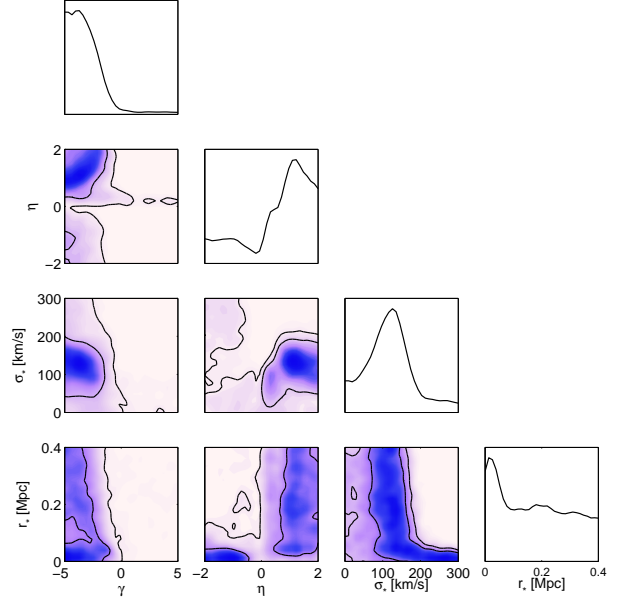


**Figure 5.** 1D and 2D marginalised posteriors distributions for the parameters  $\mathbf{h} = \{\gamma, \eta, \sigma_*, r_*\}$  of the truncated SIS halo model, derived from the analysis of real SNLS3 data.

parameters constraints lie mid-way between those obtained for the simulated SNIa data with 162 and 500 supernovae respectively, as discussed in Section 5.

Focussing on the 1D marginal posterior distribution of each halo parameter, we first note the strong preference for negative values of  $\gamma$ , as we observed in the analysis of simulations containing no lensing signal. As explained in Section 5, this is merely a consequence of the lensing signal (if any) in the data being very weak and does not constitute a meaningful constraint on the halo properties.

Conversely, there is a relatively strong preference for positive values of  $\eta$ , corresponding to a positive correlation between the halo velocity dispersion and luminosity. Indeed, the marginal distribution peaks at  $\eta \approx 1$ , which is considerably larger than the canonical values of  $\eta^p = \frac{1}{4}$  and  $\eta^{sf} = \frac{1}{3}$ , corresponding to the Faber–Jackson and Tully–Fisher relations, valid for early and late-type galaxies, respectively. This constraint also differs noticeably from that shown in the left-hand panel of Fig. 1, obtained from simulated data containing no lensing signal, which is suggestive of a marginal lensing signal being present in the real data.

The possibility of a faint lensing signal being present in the data is also suggested by the 1D marginal distribution for the fiducial velocity dispersion  $\sigma_*$ , which has a clear peak away from zero. Indeed, the peak is centred on  $\sigma_* \approx 120 \text{ km s}^{-1}$ , which was also the value assumed in the simulations analysed in Section 5. The fact that the parameter constraint obtained from the real data again appears tighter than that obtained from the simulations of 162 SNIa with no lensing signal, shown in the left-hand panel of Fig. 1, may be a result of the real data preferring  $\eta \approx 1$ , as opposed the value  $\eta = \frac{1}{3}$  used in our simulations. From (13) and (17), one sees that the lensing signal produced by a halo with a given  $\sigma_*$  is larger in the former case.

Finally, we note that the 1D marginal for the fiducial truncation radius peaks very close to zero and yields no real constraint on  $r_*$ , as we found in our analysis of the 162 simulated SNIa.

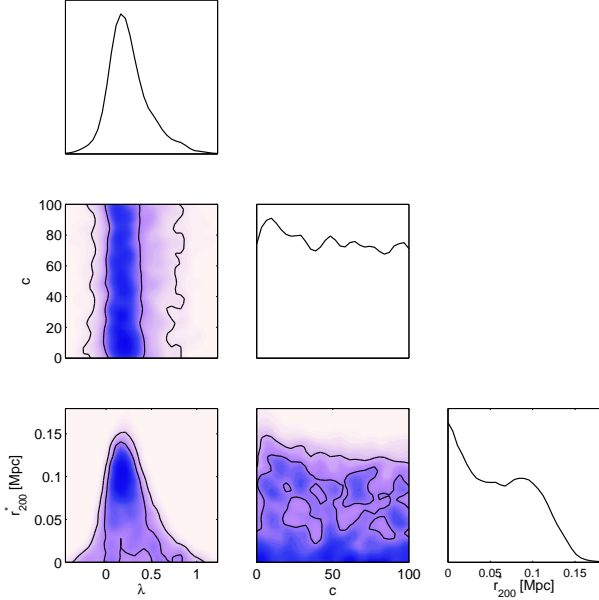


**Figure 6.** 1D and 2D marginalised posteriors distributions for the parameters  $\mathbf{h} = \{\lambda, c, r_{200}^*\}$  of the NFW halo model, derived from the analysis of real SNLS3 data.

## 6.2 NFW model

The 1D and 2D marginalised parameter constraints obtained for the NFW halo model for one galaxy type are shown in Fig. 6. The constraints on the parameters are very similar to those shown in Fig 2, obtained from 162 simulated SNIa with and without a lensing signal produced by a NFW halo model with the parameters listed in Table 3. One sees that it is not possible to place meaningful constraints on any of the parameters, indicating the absence of a detectable lensing signal. This is consistent with the low relative evidence for this model listed in Table 6.

## 6.3 Separating passive and star-forming galaxies

So far we have assumed that the halo parameters for the truncated SIS and NFW models, respectively, are the same for different galaxy types. This may be an oversimplification and so it is of interest to split the foreground galaxies into their passive and star-forming spectral types, both of which are allowed to have independent halo parameters.

We concentrate on the truncated SIS model, since this yielded a significantly higher evidence than the NFW profile in our analysis assuming just a single galaxy type (see Table 6). The galaxies in our sample are classified as either passive or star-forming depending on their sSFR (see Section 4.2). We thus allow all the halo parameters to be different for each type of galaxy, so that the full halo parameter space becomes  $\mathbf{h} = \{\gamma^p, \eta^p, \sigma_*^p, r_*^p, \gamma^{sf}, \eta^{sf}, \sigma_*^{sf}, r_*^{sf}\}$ . The fraction of passive galaxies ranges from 5 per cent in the CFHTLS fields D1 and D3 to 8 per cent in field D4. Thus, the vast majority of foreground galaxies are star-forming.

The resulting 1D and 2D marginalised posteriors for the parameters are shown in Fig. 7. One sees that the constraints on the parameters for passive and star-forming galaxies are very different. As one might expect, given the relative percentages of passive and star-forming galaxies in the catalogue, the constraints on the halo parameters of the passive galaxies are very much weaker than

those for star-forming galaxies. Indeed, for the passive galaxies, the marginal distributions closely resemble those shown in Fig. 1, obtained from simulations containing 162 SNIa with no lensing signal. Conversely, for star-forming galaxies, the constraints are slightly tighter than those shown in Fig. 5, obtained from the real data assuming just one galaxy type, but resemble them in their main features. In particular, we again see a strong preference for negative values of  $\gamma^{sf}$ , but now the 1D marginal distribution has a modest peak at  $\gamma^{sf} \approx -3$ . We also recover a strong constraint that  $\eta^{sf}$  is positive, with the 1D marginal possessing a small peak at  $\eta^{sf} \approx 1$ . The 1D marginal for  $\sigma_*^{sf}$  peaks strongly away from zero, preferring a value of  $\sigma_*^{sf} \approx 150 \text{ km s}^{-1}$ . There is, however, no constraint on  $r_*^{sf}$ , which is in keeping with our previous findings.

Finally, it is worth noting that the 2D marginal in the  $(\sigma_*^p, \sigma_*^{sf})$ -space shown in Fig. 7 bears a passing resemblance to the corresponding plot (figure 6) in Jönsson et al. (2010b), but only if  $\sigma_*^p$  and  $\sigma_*^{sf}$  are interchanged. Given the relative percentages of passive and star-forming galaxies in the catalogue, it seems sensible that one should obtain a tighter constraint on  $\sigma_*^{sf}$  than  $\sigma_*^p$ , as we find in Fig. 7. By contrast, figure 6 in Jönsson et al. (2010b) shows the opposite, which suggests that they have erroneously swapped the galaxy types in their analysis.

## 6.4 Inclusion of additional low-redshift supernovae data

We also investigate the inclusion of additional, low-redshift SNIa data to our analysis as a potential means of enhancing the detection of a halo lensing signal. The rationale here is first to analyse the low- $z$  SNIa data alone, using precisely the same methodology as for the SNLS3 data, but assuming no lensing from foreground galaxy haloes. The resulting posterior distributions derived for (most of) the nuisance parameters listed in Table 1 may then be used as priors on these parameters in the subsequent analysis of the (high- $z$ ) SNLS3 data, thereby replacing the very conservative priors assumed in Table 1, which may be ‘diluting’ the lensing signal.

As our low- $z$  SNIa dataset, we use an updated version of the catalogue compiled by Sullivan et al. (2010). This consists of a sample from the compilation of Conley et al. (2010), which itself includes SNIa from a variety of sources (primarily Hamuy et al. 1996a; Riess et al. 1999; Jha et al. 2006; Hicken et al. 2009a; Contreras et al. 2009). Sullivan et al. apply bulk-flow peculiar velocity corrections to the SN magnitudes and redshifts, placing the redshifts in the CMB-frame ( $z_{\text{cmb}}$ ) following Neill et al. (2007), but with updated models (Conley et al. 2010). Only SN Ia in the smooth Hubble flow, defined as  $z_{\text{cmb}} > 0.01$  are used, and the same light curve quality cuts as for the SNLS3 sample are employed. There are 123 low-redshift SN Ia in total, with redshifts in the range  $[0.01, 0.08]$ .

Analysis of these data yields approximately Gaussian posteriors (truncated to positive values) on the nuisance parameters, given by:  $\alpha \sim \mathcal{N}(1.30, 0.11^2)$ ,  $\beta \sim \mathcal{N}(2.81, 0.18^2)$ ,  $R_x \sim \mathcal{N}(0.119, 0.008^2)$  and  $R_c \sim \mathcal{N}(0.074, 0.05^2)$ . These distributions are clearly much tighter than the original assumed priors given in Table 1; note that we use the original prior on the nuisance parameter  $\sigma_{\text{int}}$ , as this quantity is likely to differ between low- $z$  and high- $z$  SNIa, since observational uncertainties such as the estimation of photometric errors can lead to variations of  $\sigma_{\text{int}}$  on a sample-by-sample basis (March et al. 2012). We find that using the posteriors derived from the low- $z$  SNIa as priors in the subsequent analysis of the high- $z$  SNLS3 data yields parameter constraints that are almost identical to those presented in Figs 5–7. Moreover, the log-evidences relative to the null (no-lensing) model are found to

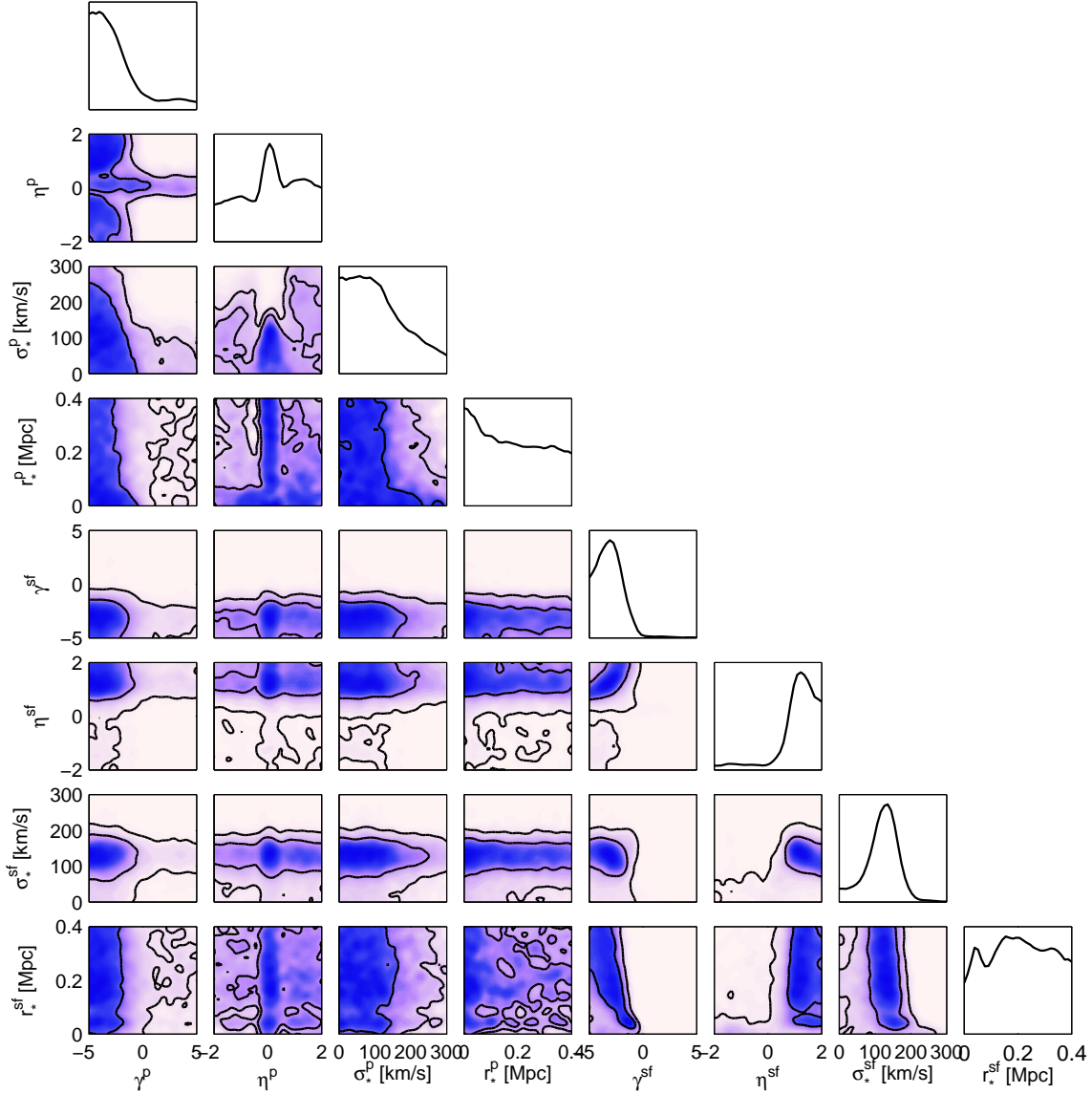


**Figure 7.** 1D and 2D marginalised posterior distributions for the parameters  $\mathbf{h} = \{\gamma^p, \eta^p, \sigma_*^p, r_*^p, \gamma^{sf}, \eta^{sf}, \sigma_*^{sf}, r_*^{sf}\}$  of the truncated SIS halo model for passive and star-forming galaxies, respectively, derived from the analysis of real SNLS3 data.

be very similar to those listed in Table 6. This finding makes sense, since the new, tighter priors on the nuisance parameters are used for both the halo and null (no-lensing) models, and they are, in fact, consistent with the posteriors derived on these parameters from the SNLS3 data alone. Thus, in summary, our results are unchanged by the inclusion of low- $z$  SNIa data.

## 7 CONCLUSIONS

We have presented a Bayesian statistical methodology for constraining the properties of dark matter haloes of foreground galaxies that intersect the lines-of-sight towards SNIa. The method builds upon the Bayesian hierarchical model presented by March et al. (2011) for improving constraints on cosmological parameters from SNIa observations. Compared with the usual  $\chi^2$ -method, which suffers from shortcomings in terms of its statistical foundations and robustness, March et al. (2011) demonstrate that

the Bayesian method delivers tighter statistical constraints, reduces statistical bias and produces confidence intervals with better statistical coverage.

We use this methodology to obtain an effective likelihood function giving the probability of obtaining the observed SNIa data (i.e. the parameter values obtained in SALT-II lightcurve fits) as a function of the parameters of the dark matter halo models assumed for the galaxies along the lines-of-sight to the SNIa. Following the imposition of suitable priors on these parameters (together with some nuisance parameters), we explore the full posterior distribution in all the parameters simultaneously using the nested sampling algorithm MULTINEST, which also calculates the Bayesian evidence for use in model comparison.

We first apply our method to simulated SNIa datasets generated using 162 high-redshift ( $0.1 \lesssim z \lesssim 1$ ) SNIa from the 3-year data release of the Supernova Legacy Survey (SNLS3) as a template and assuming either a truncated singular isothermal sphere (SIS) model or a Navarro–Frenk–White (NFW) model for

the dark matter halo density profile of foreground galaxies in the deep Canada-France-Hawaii Telescope Legacy Survey (CFHTLS) fields. These simulations were generated using the SNANA package, assuming realistic values for the halo parameters and observational data quality. Assuming conservative priors on the parameters, we demonstrate that one cannot obtain a detection of the lensing signal in this case. By considering instead a simulation catalogue containing 500 SNIa, we show that our method produces posterior distributions for the parameters that are fully consistent with their input values in the simulations. Moreover, in each case, the Bayesian evidence for the correct class of halo model far exceeds that of the no-lensing model, indicating a strong detection of the simulated lensing signal. We also analyse each simulation assuming the other (incorrect) class of halo model and show that the Bayesian evidence is able to select the correct model in each case, albeit only marginally.

In the analysis of real SNLS3 data (consisting of 162 SNIa) we find, contrary to previous studies, only a very marginal detection of a lensing signal in the case of the truncated SIS halo model, which is preferred by just 0.2 log-evidence units relative to the no lensing model. Indeed, since this difference is similar to the uncertainty in the evaluation of the evidence, one may consider the no lensing model to be equally favoured by the data. Nonetheless, the parameter constraints for the truncated SIS halo model do appear somewhat tighter than those obtained for simulations of 162 SNIa without the inclusion of a lensing signal, which is again suggestive of a borderline detection of a lensing signal in the real SNLS3 data. One finds that the SNLS3 data strongly prefer negative values of  $\gamma$ , which corresponds to luminous galaxies having smaller truncation radii than less luminous ones, but this is simply a manifestation of the lensing signal being very weak and does not constitute a meaningful constraint on the halo properties. There is also a preference for positive values of  $\eta$ , corresponding to a positive correlation between the halo velocity dispersion and luminosity, with the 1D marginal for this parameter peaking at  $\eta \approx 1$ , which is somewhat larger than the canonical values of  $\eta^p = \frac{1}{4}$  and  $\eta^{sf} = \frac{1}{3}$  valid for early and late-type galaxies, respectively, and leads to a stronger lensing signal for a halo with a given luminosity. The 1D marginal distribution for the fiducial velocity dispersion  $\sigma_*$  has a clear peak away from zero, which is centred on  $\sigma_* \approx 120 \text{ km s}^{-1}$ , but the marginal for the fiducial truncation radius peaks very close to zero and yields no real constraint on  $r_*$ . No detection or meaningful halo parameter constraints are obtained for the NFW model.

Finally, we investigate the possibility that the halo parameters may be different for passive and star-formation galaxies, respectively. Focussing on the truncated SIS model, we find that allowing all the halo parameters for the two galaxy types to be completely independent increases the evidence for the model slightly, by 0.3 log-evidence units. Since only around 5 per cent of the galaxies in our catalogue are passive, we find that one cannot place any meaningful constraints on their halo properties, but that the constraints on the halo parameters of the star-forming galaxies are similar to those obtained if one assumes just one galaxy type.

Our results contradict to some extent the previously reported high-significance detections of gravitational lensing of SNIa (Jönsson et al. 2007; Kronborg et al. 2010; Jönsson et al. 2010a,b), where the last study uses essentially the same SNLS3 data as those analysed here. We have also verified that our findings are unchanged by the inclusion of additional low- $z$  SNIa data. The major difference between these earlier analyses and the study presented here is the statistical methodology employed. As demonstrated by March et al. (2011), the usual  $\chi^2$ -method used in previous analy-

ses has a number of shortcomings in terms of its statistical foundations and robustness, including not allowing for rigorous model checking and not providing a reliable framework for the evaluation of systematic uncertainties. This should be contrasted with the statistically-principled and rigorous Bayesian hierarchical model used here. Moreover, previous studies employed using simple gridding methods to explore the parameter space of the dark matter halo models, which allow only a small subset of the parameters to be varied simultaneously.

It should be mentioned, however, that the analysis presented here does make the significant simplifying assumption that all dark matter haloes of the foreground galaxies have the same values for their free parameters (at least within their spectral type). This is not too restrictive an assumption for free parameters corresponding to fiducial values appearing in scaling laws, but it is certainly a substantial oversimplification for physical parameters such as the concentration  $c$  in the NFW profile. This may weaken the constraints in the analysis of real data, as compared with the analysis of simulated data generated assuming all the haloes to have the same parameter values. We will investigate this possibility in a future work.

In closing, we note that the analysis code used in this paper is quite general in nature and could easily be applied to other combinations of SNIa and foreground galaxy catalogues. Anyone wishing to use the code in collaboration should contact the authors.

## ACKNOWLEDGEMENTS

NVK thanks Jakob Jönsson for his invaluable help in the initial stages of this work, Mark Sullivan for providing the foreground galaxy catalogues and for many useful discussions, Ariel Goobar for reading through an early draft of the paper and providing insightful comments, and Joakim Edsjo for his support and encouragement throughout. NVK also acknowledges support from the Swedish Research Council (contract No. 621-2010-3301). MCM thanks Rick Kessler and John Marriner for assistance with simulating and analyzing SNANA data. FF is supported by a Research Fellowship from Trinity Hall, Cambridge.

## REFERENCES

- Astier P., et al., 2006, *A&A*, 447, 31
- Balland C., et al., 2009, *A&A*, 507, 85
- Bartelmann M., 1996, *A&A*, 313, 697
- Bergström L., Goliath M., Goobar A., Mörtzell E., 2000, *A&A*, 358, 13
- Boulade O., et al., 2003, in M. Iye & A. F. M. Moorwood ed., *Society of Photo-Optical Instrumentation Engineers (SPIE) Conference Series Vol. 4841 of Society of Photo-Optical Instrumentation Engineers (SPIE) Conference Series*, MegaCam: the new Canada-France-Hawaii Telescope wide-field imaging camera. pp 72–81
- Bridges M., Feroz F., Hobson M. P., Lasenby A. N., 2009, *MNRAS*, 400, 1075
- Bronder T. J., et al., 2008, *A&A*, 477, 717
- Conley A., et al., 2006, *ApJ*, 644, 1
- Conley A., et al., 2011, *ApJS*, 192, 1
- Dodelson S., Vallinotto A., 2006, *Phys.Rev.D*, 74, 063515
- Faber S. M., Jackson R. E., 1976, *ApJ*, 204, 668
- Feroz F., Balan S. T., Hobson M. P., 2011, *MNRAS*, 415, 3462

- Feroz F., Gair J. R., Graff P., Hobson M. P., Lasenby A., 2010, *Classical and Quantum Gravity*, 27, 075010
- Feroz F., Hobson M. P., 2008, *MNRAS*, 384, 449
- Feroz F., Hobson M. P., 2011, *MNRAS*, p. 2013
- Feroz F., Hobson M. P., Bridges M., 2009, *MNRAS*, 398, 1601
- Frieman J. A., 1996, *Comments on Astrophysics*, 18, 323
- Guy J., Astier P., Baumont S., Hardin D., Pain R., Regnault Ruhlmann-Kleider V., 2007, *A&A*, 466, 11
- Guy J., Sullivan M., Conley A., Regnault N., Astier P., Balland C., Basa S., Carlberg R. G., Fouchez D., Hardin D., Hook I. M., Howell D. A., Pain R., 2010, *aap*, 523, A7
- Guy J. et al., 2010, in preparation
- Hobson M. P., McLachlan C., 2003, *MNRAS*, 338, 765
- Holz D. E., Wald R. M., 1998, *Phys.Rev.D*, 58, 063501
- Howell D. A., et al., 2005, *ApJ*, 634, 1190
- Jha S., Riess A. G., Kirshner R. P., 2007, *ApJ*, 659, 122
- Jönsson J., Dahlén T., Goobar A., Mörtzell E., Riess A., 2007, *JCAP*, 6, 2
- Jönsson J., Dahlén T., Hook I., Goobar A., Mörtzell E., 2010a, *MNRAS*, 402, 526
- Jönsson J., Kronborg T., Mörtzell E., et al., 2008, *A&A*, 487, 467
- Jönsson J., Sullivan M., Hook I., Basa S., Carlberg R., Conley A., Fouchez D., Howell D. A., Perrett K., Pritchett C., 2010b, *MNRAS*, 405, 535
- Kantowski R., Vaughan T., Branch D., 1995, *ApJ*, 447, 35
- Kessler R., et al., 2009, *arXiv:0908.4280*
- Kleinheinrich M., Schneider P., Rix H. ., Erben T., Wolf C., Schirmer M., Meisenheimer K., Borch A., Dye S., Kovacs Z., Wisotzki L., 2004, *ArXiv Astrophysics e-prints*
- Kowalski M., et al., 2008
- Kronborg T., et al., 2010, *A&A*, 514, A44
- Liddle A. R., 2007, *MNRAS*, 377, L74
- Mandel K., Kirshner R. P., Narayan G., Wood-Vasey W. M., Friedman A. S., Hicken M., 2010, in *American Astronomical Society Meeting Abstracts Vol. 42 of Bulletin of the American Astronomical Society, Type Ia Supernova Light Curve Inference: Hierarchical Models for Nearby SN Ia in the Optical and Near Infrared*, p. 343.05
- Mandel K. S., Wood-Vasey W. M., Friedman A. S., Kirshner R. P., 2009, *ApJ*, 704, 629
- March M. C., Trotta R., Berkes P., Starkman G. D., Vaudrevange P. M., 2011, *MNRAS*, 418, 2308
- March M.C. et al., 2012, in preparation
- Metcalf R. B., 1999, *MNRAS*, 305, 746
- Metcalf R. B., Silk J., 1999, *ApJ*, 519, L1
- Navarro J. F., Frenk C. S., White S. D. M., 1997, *ApJ*, 490, 493
- Perrett K., Balam D., Sullivan M., Pritchett C., Conley A., Carlberg R., Astier P., Balland C., Basa S., Fouchez D., Guy J., Hardin D., Hook I. M., Howell D. A., Pain R., Regnault N., 2010, *aj*, 140, 518
- Phillips M. M., 1993, *ApJ*, 413, L105
- Rauch K. P., 1991, *ApJ*, 374, 83
- Riess A. G., et al., 2004, *ApJ*, 607, 665
- Riess A. G., et al., 2007, *ApJ*, 659, 98
- Sarkar D., Amblard A., Holz D. E., Cooray A., 2008, *ApJ*, 678, 1
- Schneider P., Ehlers J., Falco E. E., 1992, *Gravitational Lenses*
- Skilling J., 2004, in *Fischer R., Preuss R., Toussaint U. V., eds, American Institute of Physics Conference Series Nested Sampling*, pp 395–405
- Springel V., Wang J., Vogelsberger M., Ludlow A., Jenkins A., Helmi A., Navarro J. F., Frenk C. S., White S. D. M., 2008, *MNRAS*, 391, 1685
- Strolger L.-G., et al., 2004, *ApJ*, 613, 200
- Sullivan M., Le Borgne D., Pritchett C. J., Hodsman A., Neill J. D., Howell D. A., Carlberg R. G., Astier P., Aubourg E., Balam D., Basa S., Conley A., Fabbro J., Ellis R. S., Filiol M., Lusset V., Perlmutter S., Ripoche P., Tao C., 2006, *ApJ*, 648, 868
- Trotta R., 2007, *MNRAS*, 378, 72
- Tully R. B., Fisher J. R., 1977, *A&A*, 54, 661
- Wambsganss J., Cen R., Xu G., Ostriker J. P., 1997, *ApJ*, 475, L81
- Wang L., Goldhaber G., Aldering G., Perlmutter S., 2003, *ApJ*, 590, 944
- Zentner A. R., Bhattacharya S., 2009, *ApJ*, 693, 1543